Helmholtz-Zentrum Dresden-Rossendorf (HZDR)

Experimental and numerical investigations of Ni–Co–SiO2 alloy films deposited by magnetic-field-assisted jet plating

Jiang, W.; Huang, M.; Lao, Y.; Yang, X.; Wang, C.; Tian, Z.; Zhou, S.; Mutschke, G.; Eckert, K.;

Perma-Link to Publication Repository of HZDR:

https://www.hzdr.de/publications/Publ-33014

Experimental and numerical investigations of Ni–Co–SiO₂ alloy films deposited by magnetic-field-assisted jet plating

Wei Jiang[1,2,3,4,§,*], Mengyuan Huang[1,3,§], Yuanxia Lao[5,6,*], Xuegeng Yang[1,3], Changan Wang[5,7], Zongjun Tian[4], Shengqiang Zhou[5], Gerd Mutschke[1], Kerstin Eckert[1,3].

[1] *Institute of Fluid Dynamics, Helmholtz-Zentrum Dresden-Rossendorf, 01328 Dresden, Germany*

[2] *School of Mechanical Engineering, Hefei University of Technology, 230009 Hefei, China*

[3] *Institute of Process Engineering, Technische Universität Dresden, 01069 Dresden, Germany*

[4] *College of Mechanical and Electrical Engineering, Nanjing University of Aeronautics and Astronautics, 210016 Nanjing, China*

[5] *Institute of Ion Beam Physics and Materials Research, Helmholtz-Zentrum Dresden-Rossendorf, 01328 Dresden, Germany*

[6] *Guangxi Key Laboratory of Natural Polymer Chemistry and Physics, College of Chemistry and Materials, Nanning Normal University, 530001 Nanning, China*

[7] *Institute of Semiconductors, Guangdong Academy of Sciences, Guangzhou 510650, China*

* Corresponding author: ljjw737@gmail.com, 18656081809@163.com.

§ These authors contributed equally to this work.

Abstract:

A new method of magnetic-field-assisted jet plating is presented to manufacture Ni-Co-SiO₂ alloy films. The influence of different concentrations of Co^{2+} ions of the electrolyte is investigated with and without magnetic field to study the resulting properties of the deposits. The texture orientation, surface morphology, magnetic properties and corrosion resistance of the alloy films were characterized. The results show that with increasing Co^{2+} concentration in conventional jet-plating, the surface morphology changes from a granular crystal structure to a needle-like structure at 30 g/L caused by the hexagonal close-packed (HCP) structure of a large Co content. Differently, the assistance of the magnetic field leads to lower Co content in the films, even at a high Co^{2+} concentration of 30 g/L. The deposit layer remains in the face-centered cubic (FCC) structure and shows a granular morphology. The magnetic field in general leads to grain refinement and inhibits the abnormal Ni–Co co-deposition. The Ni–Co–SiO₂ alloy films obtained by magnetic-field-assisted jet plating have a smooth and dense surface. The best soft magnetic properties and corrosion resistance are obtained at a Co^{2+} concentration of 20 g/L. The coercivity is as low as 7.5 Oe, and the corrosion current density is as low as 1.12 μA·cm⁻² in 3.5 wt% NaCl solution without agitation and at room temperature, clearly showing the advantages of the method for preparing superior soft magnetic materials. In addition, a physical model of magnetic-field-assisted jet plating is established. The magnetic forces and the resulting electrolyte flow are analyzed with the help of numerical simulations, and the influence of the magnetic field on the deposition process is discussed from the perspective of magnetohydrodynamics.

1 Introduction

Soft magnetic metal composites are key materials for power electronics components and are widely used in important fields such as energy, information and transportation [1-3]. Films of Ni–Co alloy, an important ferromagnetic material, show a unique combination of high saturation magnetization, mechanic flexibility and corrosion resistance. Therefore, the field of high-density magnetic recording, which has been widely studied in recent years [5-11], continues to have good prospects for future applications.

At present, the techniques for preparing Ni–Co alloy films mainly consist of magnetron sputtering 6-8], electroless plating [9-11], and electroplating [12-21]. The sputtering method requires expensive equipment, and the obtained thin films have a relatively large grain size and a poor compactness [7, 8]. Alternatively, electroplating methods have proven to deliver high-density, high-temperature-resistant, nanocrystalline materials with strong wear resistance and corrosion resistance, if the processing parameters are properly adjusted [12-18]. As, it is a simple, low-cost process, it meanwhile became and an important method for preparing nano-scale Ni–Co alloy films in industry. S. Vilain et al. [18] studied the correlation between surface roughness, composition and magnetic properties of Ni–Co layers, and the coercivity was found to decline when the film surface roughness was reduced within a certain range. A. Karpuz et al. [19] found that the coercivity of Ni–Co films decreases with increasing film thickness due to the change in the preferred crystal orientation. S. Meena et al. [20] studied the influence of Cr doping on the structure, morphology, mechanical and magnetic properties of Ni–Co–Cr alloy films, revealing that a film doped with a high concentration of Cr has the highest hardness. U. Sarac et al. [21] discussed the observation that coercivity and remanence of the Ni–Co films decrease as the current density applied during deposition increases. The above studies indicate that the properties of Ni–Co films are very sensitive to the parameters of the manufacturing processes. For a recent review of Ni-Co composite electroplating, we refer to [4].

Jet plating is a special electroplating method that uses fast electrolyte circulation. It has the characteristics of high efficiency, fast deposition speed, and selective deposition. Jet plating is widely used in the preparation of nanomaterials [22-24]. A disadvantage is that tip discharge effects may occur at higher current densities, resulting in a decrease in the flatness and uniformity of the deposited films. Compared with electroless and traditional plating methods, the magnetic field-assisted jet electroplating method can achieve higher deposition rates at higher current densities, thereby significantly improving the density and uniformity of the film. Furthermore, its process equipment is simple, and it is a new type of green and environmentally friendly remanufacturing technology [23, 24].

Earlier research has shown that in jet-plating adding nanoparticles can effectively improve the surface morphology and refine the grain growth of Ni–Co composite films [23, 25]. However, the magnetic properties of these films were not yet investigated. In the present work, a small number of SiO$_2$ nano-particles was added to the electrolyte to inhibit the growth of Ni and Co grains in the Ni–Co alloy. Magnetic-field-assisted jet plating of Ni–Co–SiO$_2$ alloy films was performed to study the abnormal co-deposition of Ni–Co under the action of a magnetic field. Electrolytes of different Co^{2+} concentration were used, and the analysis

of the films obtained focuses on the aspects of texture orientation, surface morphology, magnetic properties and corrosion resistance with respect to the impact of the magnetic field. In addition, we performed numerical simulations to explore how the magnetic field influences the process of magnetic-field-assisted jet plating. Examining the electrolyte flow modified by the magnetic forces, including the Lorentz force and the magnetic gradient force, helps to better understand the mass transport of the metal ions near the electrode and the mechanism behind the growth of the deposit in magnetic-field-assisted jet plating.

2 Methods

2.1 Experimental setup

Fig. 1a shows a diagram of the magnetic-field-assisted jet plating system and Fig. 1b is a photograph of the experimental setup, which mainly consists of a power supply, control motor, heating equipment and jet plating area. The heating equipment was used to heat the plating bath to maintain a stable temperature during the jet plating. The motor was controlled to realize the reciprocating movement between the nozzle and the sample. The experiment was carried out at a constant potential. The nickel rod in the jet plating area was connected to the anode of the power supply, and the back of the sample to be plated was connected to the cathode of the power supply. The electrolyte was recycled in the experimental system; the red arrow indicates the direction of electrolyte circulation, which is different from traditional electroplating. Filter meshes were installed at the electrolyte inlet and outlet to prevent solid particles and other impurities from reaching the electrode surface during the jet plating and affecting the plating stability. Before the deposition experiments, nano-SiO_2 particles were well mixed into the electrolyte by magnetic stirring and ultrasonic agitation for 6 hours, and no obvious nanoparticles sedimentation in the electrolytic cell could be observed. The magnetic field in the experiment was provided by a pair of horizontally placed NdFeB (N45) magnets with a size of $30 \times 30 \times 15$ mm. As the electrolyte flow was directed vertically downward, the electric field was perpendicular to the direction of the magnetic field. Fig. 1c shows the distribution of magnetic lines. The magnetic field near the magnet surface is about 0.4 T. This field only becomes stronger near the edges of the magnets, resulting in a non-uniform magnetic field in the machining gap. Fig. 1d indicates the geometry and boundary conditions in the 3D numerical simulations of the electrolyte flow. For detailed information, see Section 3.5.

(a) System diagram of the magnetic-field-assisted jet plating   (b) Experimental setup

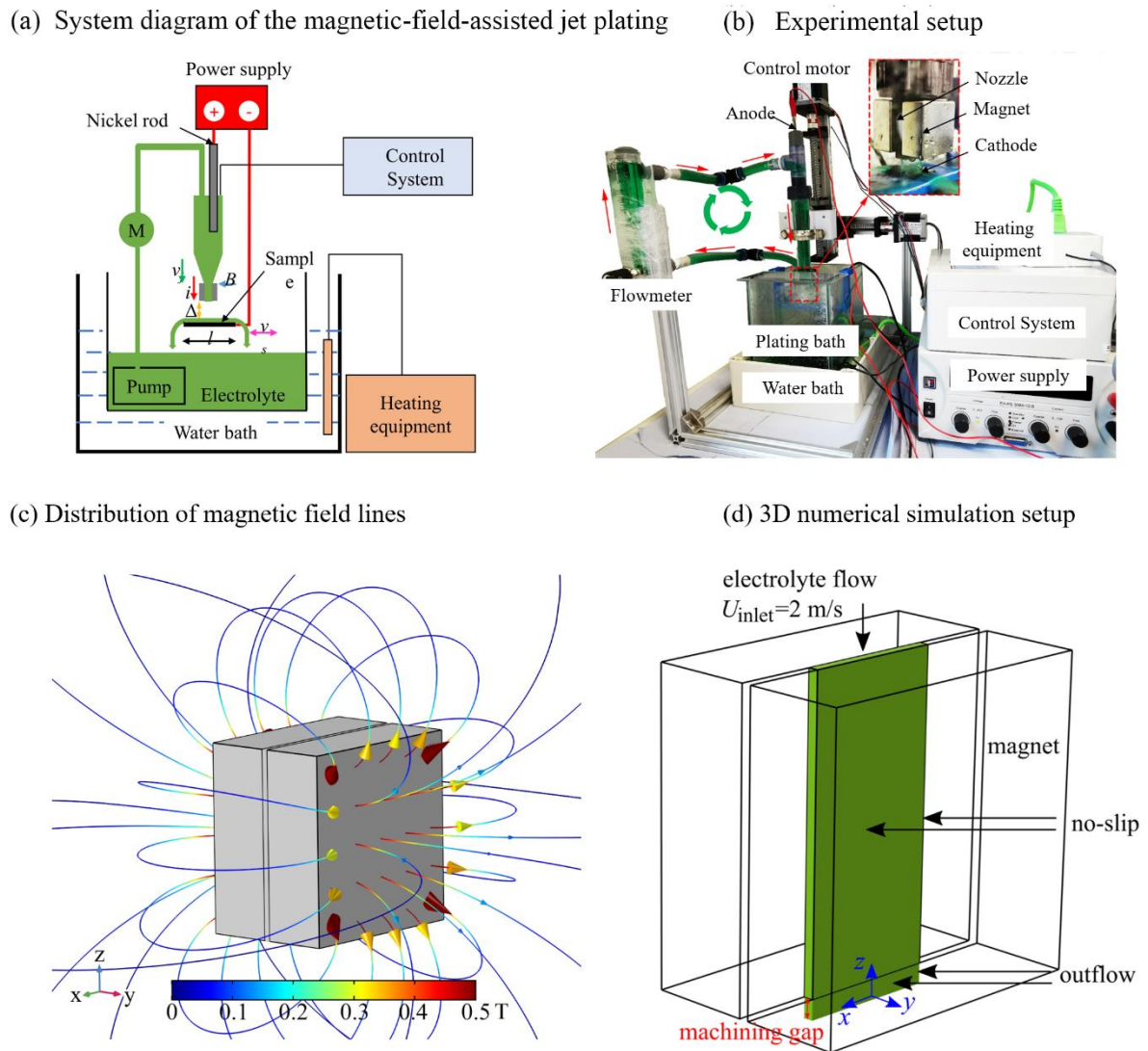(c) Distribution of magnetic field lines   (d) 3D numerical simulation setup

Fig. 1. (a) Diagram of the magnetic-field-assisted jet plating system; (b) Photo of the experimental setup; (c) Distribution of magnetic field lines (numerical result); (d) Geometry and boundary conditions in the 3D numerical simulations of the electrolyte flow.

2.2 Experimental parameters

The compositions of the bath solutions are shown in Table 1. All the experimental reagents are analytically pure. In order to study the influence of the Co^{2+} concentrations on the plated Ni–Co alloy films, different concentrations of the Cobalt salt were added sequentially in a simple Watts electrolyte and mixed. Stainless steel size of size $20 \times 20 \times 2$ mm^3 was used as substrate, which in preparation was polished with abrasive paper and put in dilute hydrochloric acid to remove the surface oxide layer.

Table 2 shows the specific processing parameters of magnetic-field-assisted jet plating. Table 3 shows the sample numbers and corresponding processing parameters of the Ni–Co–SiO$_2$ alloy films involved in this paper. The deposition parameters of voltage, current density and electrolyte composition correspond to values used earlier in jet deposition, which were found to be optimum with respect to the deposit properties [61].

Table 1. The compositions of the bath solution.

Electrolyte composition	Contents	Application
$NiSO_4 \cdot 6H_2O$ (g/L)	280	The main source of Ni^{2+}
$CoSO_4 \cdot 6H_2O$ (g/L)	10/20/30	The main source of Co^{2+}
$NiCl_2 \cdot 6H_2O$ (g/L)	40	Remove anode polarization
SiO_2 (10nm) (g/L)	4.0	Refined composite films
H_3BO_4 (g/L)	40	Adjust pH
pH	4.2	Plating pH condition
Temperature (°C)	50	Plating temperature

Table 2. Processing parameters of magnetic-field-assisted jet plating.

Processing parameters	Contents
Magnetic flux density (B)	~0.4 T (machining gap)
Machining gap (△)	3.0 mm
Scanning speed (v_s)	6.0 mm/s
Flow rate	100 L/h
Mean flow velocity in the nozzle (v_j)	2.0 m/s
Voltage (U)	25 V
Plating time (T)	25 min

Table 3. Sample number and processing conditions.

Sample	Co^{2+} (g/L)	Magnetic field	Processing mode
a	10	No	Jet plating
b	10	Yes	Magnetic-field-assisted jet plating
c	20	No	Jet plating
d	20	Yes	Magnetic-field-assisted jet plating
e	30	No	Jet plating
f	30	Yes	Magnetic-field-assisted jet plating

2.3 Characterization

The surface morphology of the films was characterized using an Ultra-high Resolution Scanning Electron Microscope (Regulus8220) and the elemental analysis was conducted by energy-dispersive X-ray spectrometry (EDS). The films were analyzed by X-ray diffraction (XRD) on a spectrometer (DMAX-2500PC) operated at 40 kV and 150 mA with Cu-Kα radiation (λ= 0.15406 nm) to determine the phase composition and crystallite size. The films were peeled off from the substrates, then cut into 2×2 mm^2 pieces for magnetic measurements. All samples were measured with a superconducting quantum interference device (SQUID-VSM, Quantum Design). Hysteresis measurements were conducted at 300 K while the magnetic field was varied from −1 T to +1 T. The direction of the magnetic field was in the plane of the films. The corrosion resistance of the films was investigated by polarization using an electrochemical workstation (CHI660E) in a 3.5 wt% NaCl corrosive medium without agitation and at room temperature. The reference electrode was a saturated calomel electrode, and the counter electrode was made of platinum.

The reactions occurring at the cathode and the anode are the hydrogen evolution reaction and the dissolution of the metal, respectively. The samples were immersed in the corrosive medium for about 30 min to attain the open circuit potential (Eocp). Immediately afterwards, potentiodynamic sweeping was performed over the potential range of -500 mV to $+500$ mV with respect to Eocp with a sweep rate of 1 mV/s.

2.4 Numerical simulations

To better understand the magnetic field effects, we performed numerical simulations of the magnetic field and the flow velocity using the finite element software COMSOL [40, 41]. For detailed information on the numerical model, see [51]. The numerical parameters correspond to the experiments. The origin of the numerical coordinate system is chosen to be at the bottom center of the machining gap. As the strong jet flow continuously brings fresh electrolyte towards the substrate, we assume the concentration has a stationary distribution and perform steady-state simulations. The concentration is assumed to be uniform except in the concentration boundary layer with a thickness of 60 μm, where the distribution fulfills $\frac{\partial c_{\text{Ni}^{2+}}}{\partial z} = \frac{-j}{2n_{\text{Ni}^{2+}}FD_{\text{Ni}^{2+}}}$ [58]. Note that we consider only Ni^{2+} and SO_4^{2-} ions here for the sake of simplicity. Here, $j = 10000$ A/m^2 is the current density, $n_{\text{Ni}^{2+}} = 2$ is the charge number, $F = 96485$ C/mol is the Faraday constant and $D_{Ni^{2+}} = 1.2 \times 10^{-9}$ m^2/s is the diffusion constant of Ni^{2+} [44, 59]. This generates a concentration gradient on the substrate which may be important for the action of the magnetic gradient force [42, 51].

The magnetic field is calculated from Maxwell's equations; the calculated field distribution is discussed later in Fig. 8. The flow field is obtained by solving the Navier-Stokes equations supplemented by the incompressibility constraint and a turbulence model. The Reynolds number $Re = UD_{\text{H}}/v$ is estimated to be 3391, assuming that the average inlet velocity U is 2 m/s (derived from electrolyte flow rate, Table 2), the characteristic length is the hydraulic diameter of the channel of $D_{\text{H}} = 1.75$ mm, and the kinematic viscosity v is 1.032×10^{-6} m^2/s [56]. As the calculated Reynolds number is in the range of the transition from laminar to turbulent flow [57], a low Reynolds number $k - \varepsilon$ model is applied to account for the turbulence in the flow [40, 55]. Fig. 1d shows the geometry and the boundary conditions for the flow field of the simulation model. The flow has a uniform velocity of $U = 2$ m/s at the inlet, which develops when passing through the nozzle. A no-slip condition is applied at the nozzle walls and the substrate, and ambient pressure is applied at the exit of the flow channel.

3 Results and discussion

3.1 Texture orientation

The XRD patterns of Ni–Co–SiO₂ alloy films under different conditions are shown in Fig. 2, and the average grain size of each film is estimated using the Scherrer equation, as shown in Table 4. As the concentration of Co²⁺ in the electrolyte increased, the average grain size of the Ni–Co–SiO₂ alloy films first decreased, then increased. This is consistent with the results in [14]. While the smallest grain size was found to be 27.9 nm for a 20 g/L concentration without a magnetic field. When the magnetic field was applied, the average grain size was further refined to 24.5 nm. The same behavior was found in the surface roughness

measurements using a Sensofar Metrology in the Supporting Information. The diffraction patterns showed that the major phase of the Ni–Co–SiO$_2$ film had a face-centered cubic (FCC) structure, and the corresponding diffraction peaks were (111), (200), and (220). There was a slight offset between the diffraction peaks and the standard peaks (Ni: JCPDS file card # 04-0850) as the Co atoms were added to the Ni matrix in the form of replacement and solid solution [27]. Furthermore, some nano-SiO$_2$ particles doped in the Ni–Co alloy films also contribute to the lattice distortion. It should be noted that the diffraction peaks for SiO$_2$ were hardly found in Fig. 2, which may be due to the low content of SiO$_2$ in the alloy film.

The phases composite of the Ni–Co–SiO$_2$ alloy film changed distinctly as the concentration of Co^{2+} increased to 30 g/L in the electrolyte. The XRD pattern (Fig. 2) shows that sample e (30 g/L of Co^{2+}, without a magnetic field) contains the second phase of Co (marked by arrows). Unlike the other phases, with the FCC structure typical of Ni–Co solid solute, this second phase had a hexagonal close-packed (HCP) structure. This indicates that a part of the Co^{2+} was added to the Ni base in the form of a replacement, and the other part of Co^{2+} grew as a hexagonal close-packed (HCP) structure [14]. However, for sample f (30 g/L of Co, with the magnetic field), there was no Co precipitation in the hexagonal close-packed (HCP) structure. This indicates that the magnetic field can inhibit the abnormal co-deposition of Ni–Co alloy, resulting in a higher solid solubility of Co in Ni.
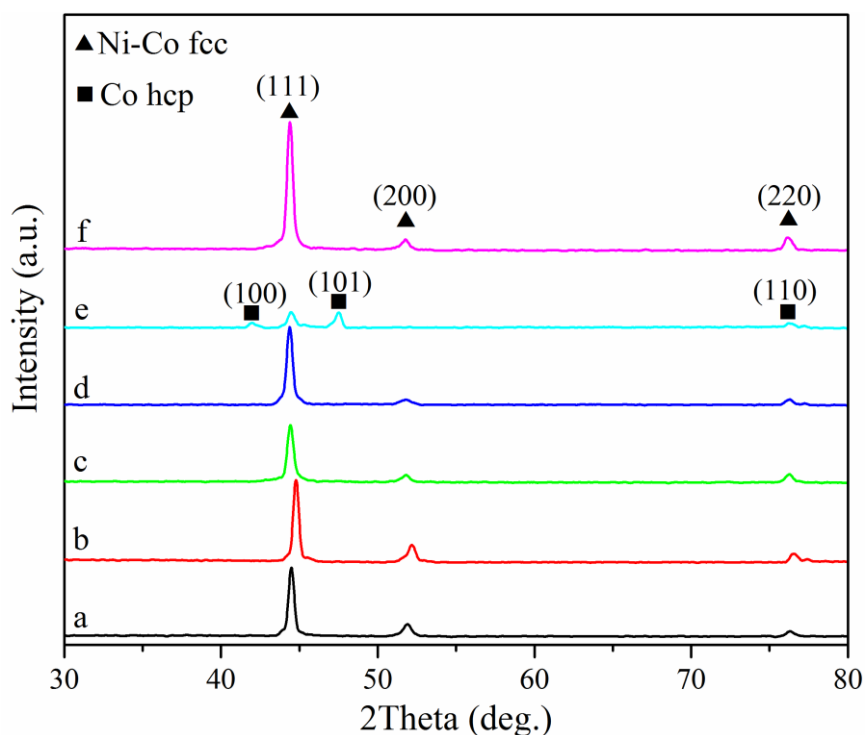

Fig. 2. XRD patterns of Ni–Co–SiO$_2$ alloy films under different conditions (see Table 3).

3.2 Surface morphologies

Fig. 3 shows the surface morphologies of Ni–Co–SiO$_2$ alloy films under different conditions. In jet plating without a magnetic field, the surface of the Ni–Co–SiO$_2$ alloy films changed significantly as the concentration of Co^{2+} increased. When the Co^{2+} concentration was as low as 10 g/L, the Ni–Co–SiO$_2$ alloy film mainly grew with a granular structure that was relatively flat and uniform, as shown in Fig. 3a. When

the Co^{2+} concentration increased to 20 g/L, a few needle-like crystal structures emerged from the original granular structure, as shown in Fig. 3c. When the Co^{2+} concentration was further increased to 30 g/L, the needle-like crystal growth prevailed in the film and the original granular structure almost disappeared. The grains became coarser and the compactness decreased between the crystal grain boundaries, as seen in Fig. 3e. The change in the surface morphology is related to the change in the crystal structure [14]. In general, as the concentration of Co^{2+} enhances, the deposition of Co^{2+} is enhanced, and the reduction of Ni^{2+} ions is reduced. This can affect the mass ratio of Co and Ni in the alloy film, and thus affect the crystal structure of the alloy. As shown in Fig. 2, an increase in the concentration of Co^{2+} (sample a→c→e) leads to an increase in the intensities of the FCC peaks and a decrease in that of the HCP peaks. With the highest Co^{2+} concentration (sample e), a mixed crystalline structure of FCC and HCP is observed. This corresponds to the change of the surface morphology from a granular structure to a needle-like structure, which is consistent with the results reported in [14].

The surface grains of the Ni–Co–SiO$_2$ alloy films with the same concentration of Co^{2+} during magnetic-field-assisted jet plating are shown in Fig. 3.b, d, f. The Ni–Co–SiO$_2$ alloy film had the best surface quality with refined grain and the highest density when the Co^{2+} concentration was 20 g/L, as depicted in Fig. 3d. In comparison with the samples without a magnetic field, the surface grains of the alloy films were refined and much denser and uniform. In Fig. 3f, especially, it is seen that the granular growth structure was still maintained without microcracks and gaps between the grain boundaries. In the electrolyte with the same Co^{2+} concentration, the magnetic field also has a certain effect on the surface morphology of the Ni–Co–SiO$_2$ film. The magnetic field can slightly enhance the mass transfer at the electrode surface and modify the growth orientation of the film, thereby improving the flatness and compactness of the deposit. For detailed discussion of the magnetic effects on the surface morphology, see Section 3.6.
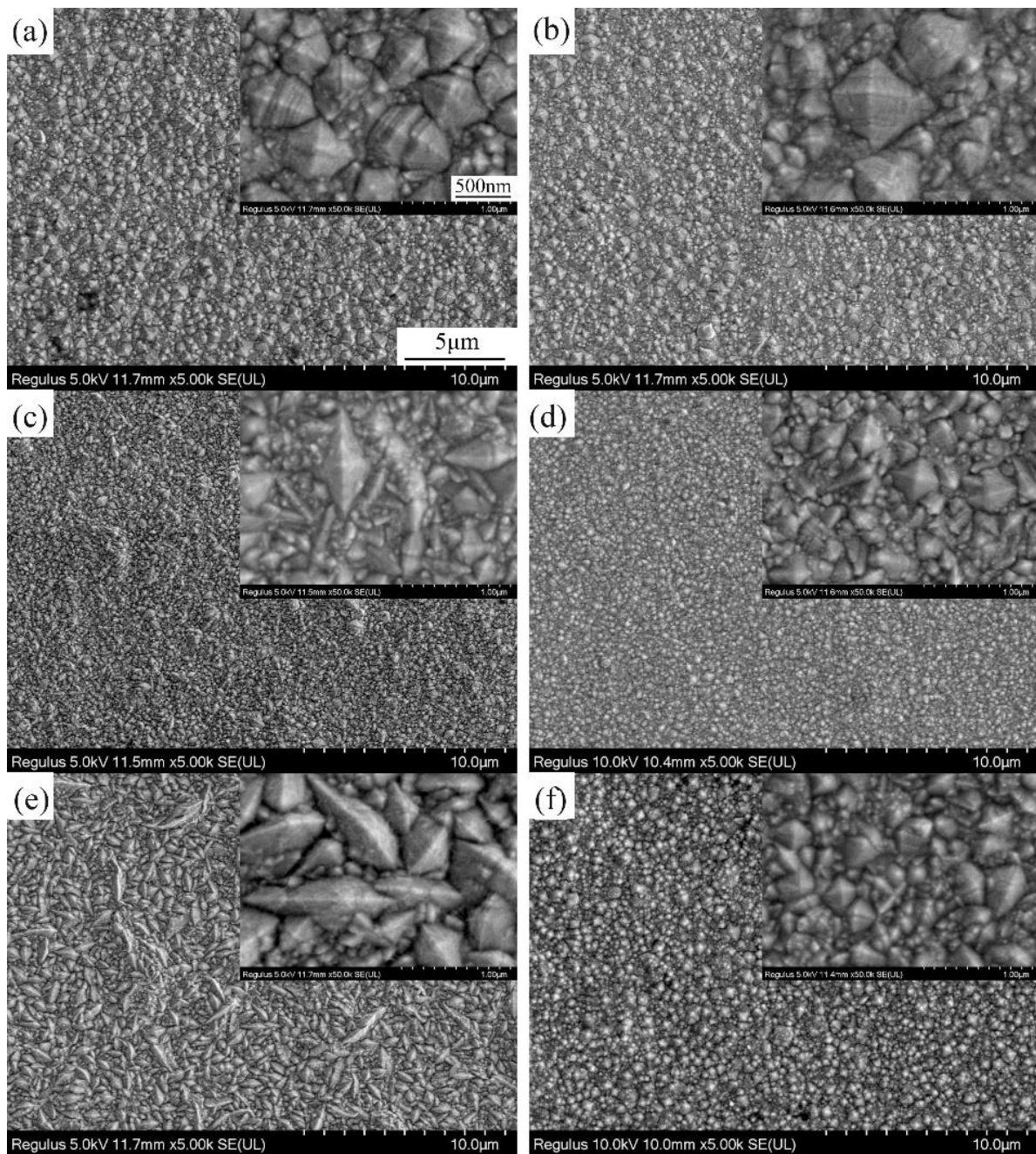
Fig. 3. Surface morphologies of Ni–Co–SiO₂ alloy films under different conditions (see Table 3).

Fig. 4 shows the distribution of elements on the surface of the Ni–Co–SiO₂ alloy film with magnetic-field-assisted jet plating for the Co²⁺ concentration of 20 g/L. It can be seen that the elements in the Ni–Co–SiO₂ alloy film were uniformly distributed and the nano-SiO₂ particles were successfully embedded in the alloy film [26].
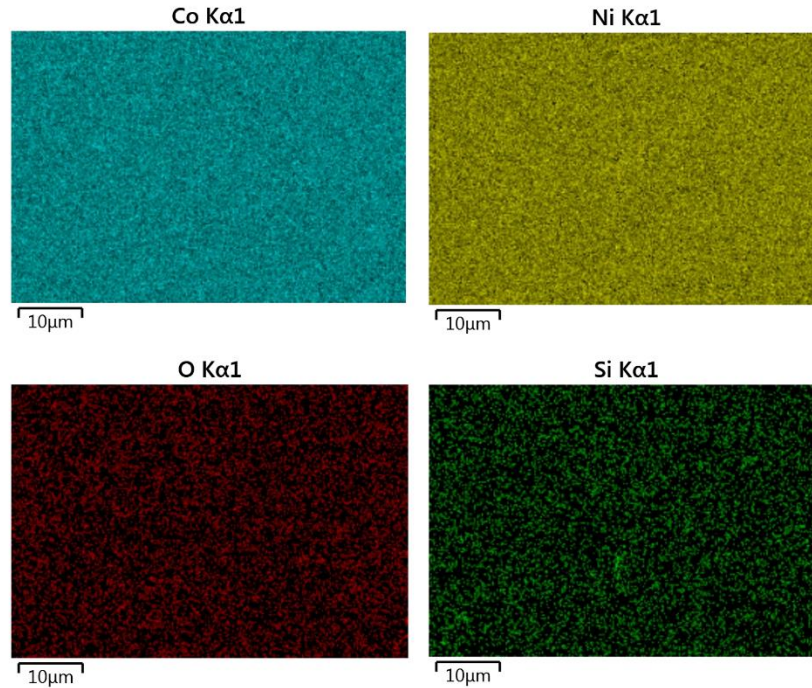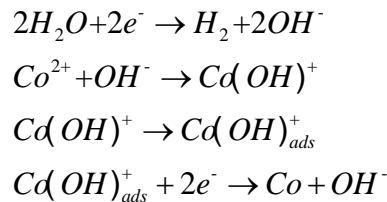
Fig. 4. Distribution of elements on the surface of the Ni–Co–SiO$_2$ film in magnetic-field-assisted jet plating.

Fig. 5 shows the ratio of Ni and Co elements in different Ni–Co–SiO$_2$ films analyzed by EDS. The mass ratio of Co and Ni in the films without a magnetic field (denoted by a, c, e in Fig. 5) was found to be much higher than the mass ratio of Co^{2+} and Ni^{2+} in the electrolyte, especially for sample e which contained twice as much Co as Ni, although the standard electrode potential for depositing Co (-0.28 V) is more negative than that for depositing Ni (-0.26 V) [44]. The high content of Co in the Ni-Co alloy indicates an abnormal co-deposition. Similar studies have shown that abnormal co-deposition also occurred during the co-deposition of iron group metals (Fe, Co, Ni) and Zn with iron-group metals [28-31]. The abnormal co-deposition shown in Fig. 5 indicates the formation of hydroxide of Co. The high current density used in the jet plating enhances the deposition rate, but also increases the probability of hydrogen evolution side reactions. Due to the accumulation of hydroxide ions (OH$^-$) near the electrode surface, Co^{2+} ions tend to be partly deposited as hydroxide as well, which inhibits the deposition of Ni. The reaction equation is as follows [12, 30]:

$$2H_2O + 2e^- \rightarrow H_2 + 2OH^-$$
$$Co^{2+} + OH^- \rightarrow Co(OH)^+$$
$$Co(OH)^+ \rightarrow Co(OH)^+_{ads}$$
$$Co(OH)^+_{ads} + 2e^- \rightarrow Co + OH^-$$

If there it no magnetic field, the formation of Co(OH)$_2$ and thus the mass ratio of Co in the Ni–Co alloy film strongly increased as the concentration of Co^{2+} ions in the electrolyte increased. If a magnetic field is applied, the mass ratio of Co in the alloy film is found to be lower (see b, d, f in Fig. 5), indicating that the formation of the hydroxide is suppressed. This may be caused by the electrolyte flow which is modified by

the magnetic forces. As also reported in [32], the enhanced electrolyte convection caused by the magnetic field can enhance the mass transport of the hydrogen ions towards the electrode surface, so that the increase in the pH value at the cathode surface during the deposition is not as much as in the case without a magnetic field. Therefore, the magnetic field can effectively inhibit the generation of $Co(OH)_2$, and relatively increase the deposition rate of Ni [32].
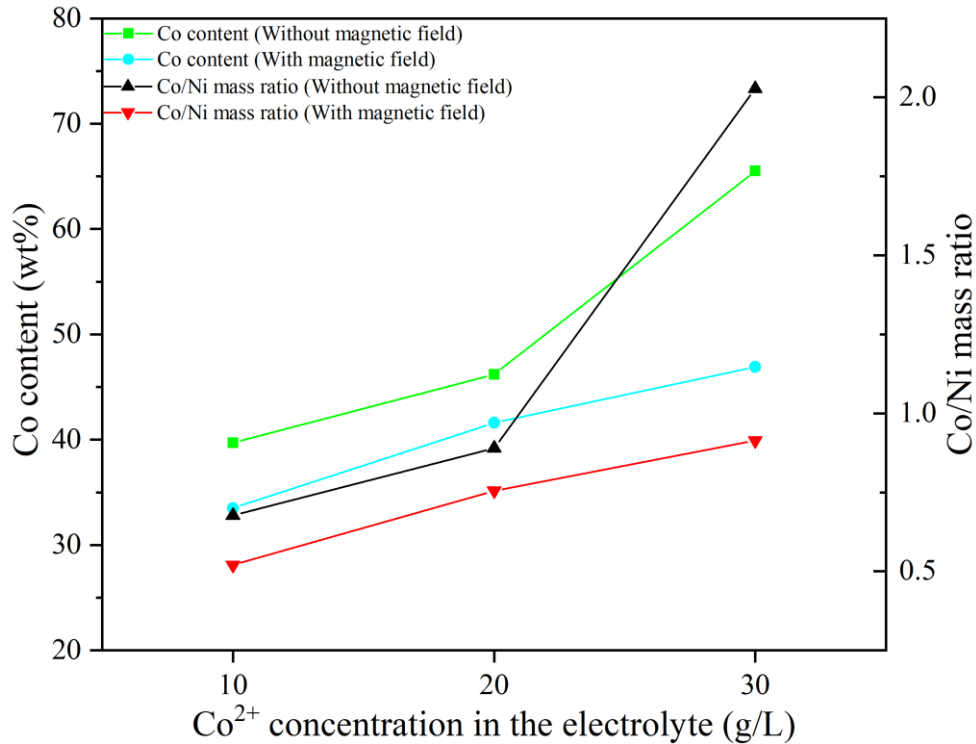

Fig. 5. The Co content and the ratio of Co to Ni in different Ni–Co–SiO$_2$ alloy films.

3.3 Magnetic properties

Fig. 6a shows the in-plane magnetic hysteresis loops of the different Ni–Co–SiO$_2$ films. Fig. 6b is a partially enlarged view of the hysteresis loop of the Ni–Co–SiO$_2$ films when the Co^{2+} concentration amounts to 30 g/L in the electrolyte. The coercivity (Hc), saturation magnetization (Ms), and residual magnetization (Mr) of each film were obtained from the magnetic hysteresis loops and are listed in Table 4, supplemented with the average grain size of the deposits. The coercivity of the films obtained by magnetic-field-assisted jet plating was always lower than the one obtained by conventional jet plating at the same Co^{2+} concentration of the electrolyte. At 20 g/L, the lowest coercivity value of 7.5 Oe was found, yielding the best soft magnetic properties. This in agreement with earlier research stating that magnetic-field-assisted jet plating is beneficial for obtaining soft magnetic materials of low coercivity [33].

With increasing Co^{2+} concentration, with or without magnetic field, the coercivity of the films first decreases and then increases again. This is closely related to the corresponding variation of the grain size, as shown in Table 4, and as also known from earlier work [34, 35].
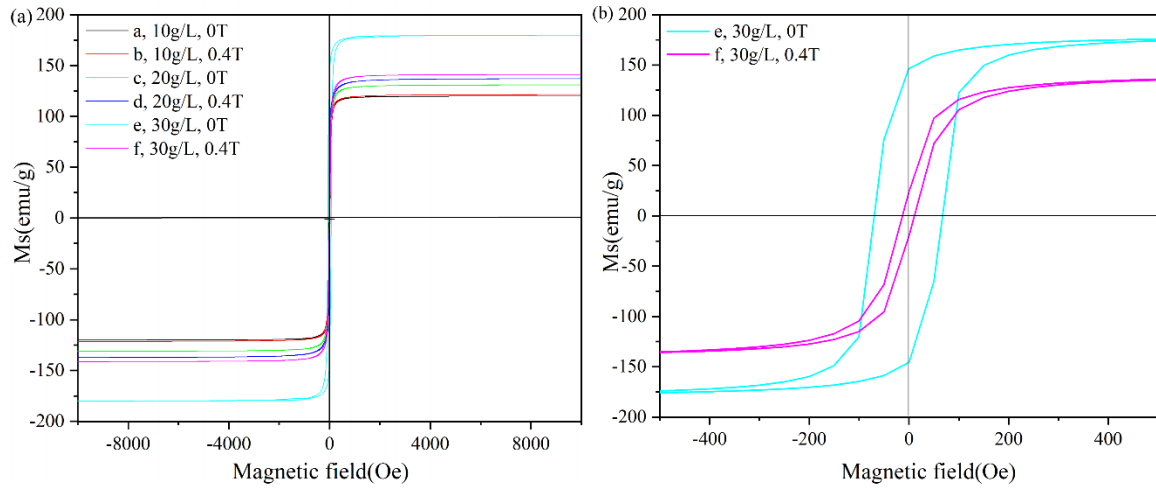
Fig. 6. (a) In-plane magnetic hysteresis loops of different Ni–Co–SiO$_2$ alloy films (see Table 3).; (b) Partially enlarged view of the Ni–Co–SiO$_2$ alloy films obtained from a Co^{2+} concentration of 30 g/L.

Table 4. Average grain size, coercivity, saturation magnetization, and remanent magnetization of the different alloy films (see Table 3).

Samples	Average grain size (nm)	Hc//(Oe)	Ms//(emu/g)	Mr//(emu/g)
a	30.6	17	119.85	50.63
b	27.9	14	121.53	38.07
c	29.3	14	131.03	28.90
d	24.5	7.5	137.17	23.17
e	32.4	71	179.65	146.82
f	29.7	10	141.23	20.11

Table 4 further shows that the saturation magnetization (Ms) increased with the Co^{2+} concentration. Because the magnetic moment of Co (1.7 μ_B/Co) is higher than that of Ni (0.6 μ_B/Ni), the increase in the Co content in the film causes an increase of the magnetic moment per unit volume. Therefore, the saturation magnetization (Ms) is closely related to the Co content in the films [12, 36]. Differently, the remanent magnetization follows the same trend as the coercivity in different Ni–Co–SiO$_2$ alloy films, which results from the close relationship between the grain size and remanent magnetization.

The above results show that the application of a magnetic field in jet plating has a great influence on the magnetic properties of the films by changing the concentration of Co and Ni, and of the grain size of the films. A significant reduction of the coercivity and the remanent magnetization improves the soft magnetic properties of the films to a large extent.

3.4 Corrosion resistance

Fig. 7 shows the polarization curves and Nyquist plots of different Ni–Co–SiO$_2$ alloy films. The electrochemical data extracted from the polarization curves and Nyquist plots of the films are listed in Table 5. In general, the corrosion potential in the Ni–Co–SiO$_2$ alloy film was shifted positively with the increase in the Co^{2+} concentration. Therefore, the increase in the Co^{2+} concentration increased the Co content in the alloy film, thereby reducing the corrosion [14, 35]. Moreover, the corrosion current density of the Ni–Co–

SiO$_2$ alloy film was further reduced when the magnetic field was applied. Thus, the corrosion resistance of the films was further enhanced at the same level of Co^{2+} concentration. From all the films investigated, the best corrosion resistance with a corrosion potential of −0.30 V and a corrosion current density of 1.12 μA·cm^{-2} was observed at a Co^{2+} concentration of 20 g/L. The polarization resistance of the alloy film also characterizes the variation of the corrosion resistance [6, 37].
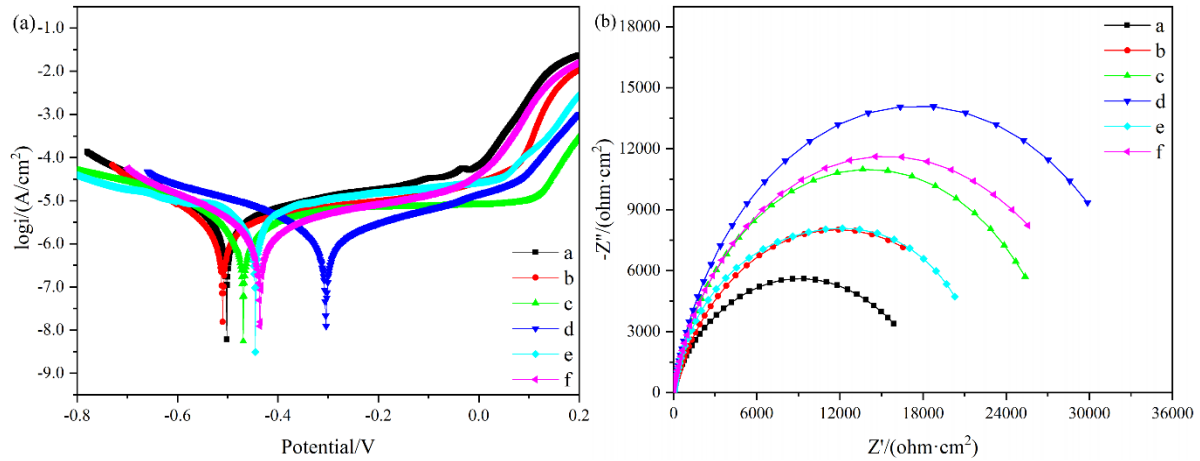

Fig. 7. (a) Polarization curves in 3.5 wt% NaCl solution; (b) Nyquist plots of the films.

Table 5. Electrochemical data extracted from the polarization curves and Nyquist plots of the films.

Sample	E_{corr}/V	i_{corr}/μA·cm^{-2}	R_p (ohm·cm^2)
a	−0.50	4.29	1.317×10^4
b	−0.51	2.15	2.570×10^4
c	−0.47	2.46	2.838×10^4
d	−0.30	1.12	3.549×10^4
e	−0.44	7.30	5.190×10^3
f	−0.43	1.89	3.229×10^4

The corrosion resistance of the Ni–Co–SiO$_2$ alloy films mainly depends on the grain size and surface morphology of the film [38]. Generally, corrosion tends to occur along the grain boundaries. Reducing the grain size is beneficial to obtain a more uniform and dense film structure on the surface, and it is harder for corrosive media to penetrate the smoother, denser film. The corrosion resistance was thus improved [39]. In the case of jet plating, the surface of the alloy film began to change from a dense granular structure to a loose needle-like crystal structure when the Co^{2+} concentration reached 30 g/L in the electrolyte. Some micro-cracks and holes appeared between the grain boundaries, as shown in Fig. 3e. Then it may be suspected that a corrosive liquid entered the film through these surface defects and caused a larger corrosion damage. In contrast, the magnetic-field-assisted jet plating improved the density of the alloy film, as shown in Fig. 3f. Therefore, the assistance of a magnetic field makes it more difficult for the corrosive medium to penetrate, thereby further enhancing the corrosion resistance of the film.

It should be noted that the corrosion properties depend on the concentration of the dissolved oxygen in the solution. Despite all corrosion measurements were done in sequence using the same solution to ensure a comparable amount of dissolved oxygen in all measurements, its approximate value is not known. An

improved oxygen control by removing the oxygen using nitrogen sparging or fixing the oxygen concentration by air saturation, accompanied by probes to monitor the concentration, will be considered in future work.

3.5 Simulation results

Fig. 8a shows the numerical results of the magnetic field distribution in the center vertical cross-section. Strong magnetic fields are found at the edges of the magnet, causing a non-uniform distribution of the magnetic field at the machining gap at the bottom (indicated by red dashed lines) where the magnetic field exerts an influence on the deposit growth. The gradients of the magnetic field along the substrate in the center vertical cross-section are shown in Fig. 8b. It is clear that the gradients mainly exist in y, z directions. The maximal gradients are found near the edges of the magnets, reaching 80 T/m. Below the nozzle, where the highest deposition takes place ($-0.5\ mm \leq y \leq 0.5\ mm$), the magnetic gradients have a magnitude of less than 20 T/m.
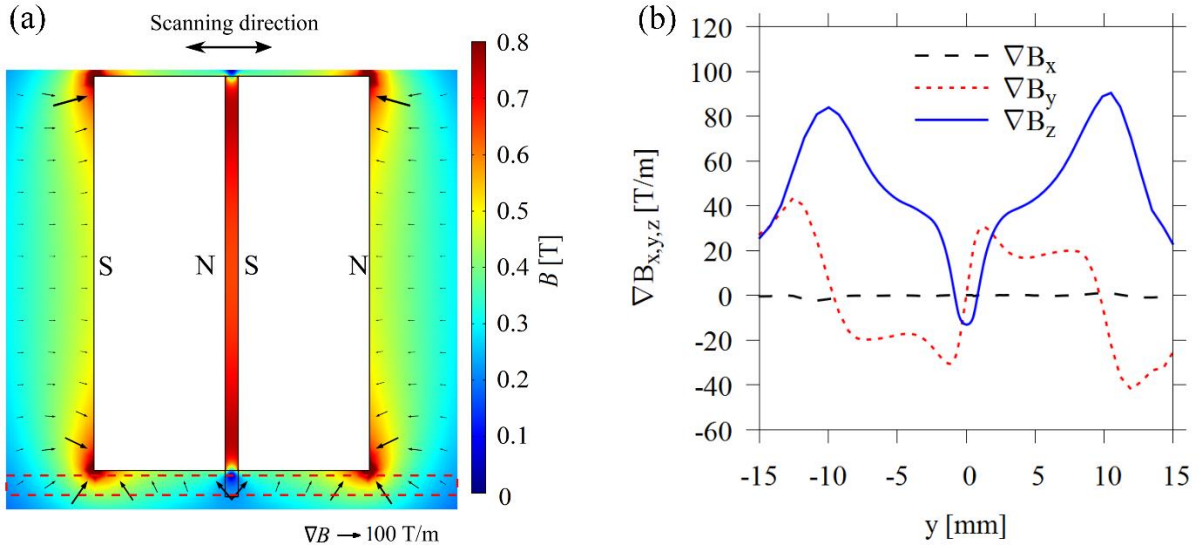

Fig. 8. (a) Color surface: magnetic field in the vertical cross-section (yz plane in Fig. 11 (a)) passing the center of the magnets. Black arrows indicate the vectors of the magnetic field gradients $\nabla \boldsymbol{B}$. Red dashed lines indicate the position of the machining gap where the deposit grows; (b) Gradients of the magnetic field along the substrate ($x = 0, z = 0\ mm$, bottom red dashed line in (a)).

The magnetic field generates a Lorentz force and a magnetic gradient force, which can drive electrolyte flow [42]:

$$\boldsymbol{f}_{\mathrm{L}} = \boldsymbol{j} \times \boldsymbol{B}. \tag{1}$$

$$\boldsymbol{f}_{\nabla \mathrm{B}} = \frac{\chi_{\mathrm{sol}}}{\mu_0}(\boldsymbol{B} \cdot \nabla)\boldsymbol{B}, \qquad \chi_{\mathrm{sol}} = \sum_i \chi_i^{\mathrm{mol}} c_i + \chi_{\mathrm{H_2O}}. \tag{2}$$

Here, $\boldsymbol{j}, \boldsymbol{B}, \mu_0, \chi_{\mathrm{sol}}, \chi_{\mathrm{H_2O}}$ denote the current density, the magnetic flux density, the magnetic susceptibility of the solution and the water, respectively. χ_i^{mol} and c_i are the molar magnetic susceptibility and the concentration of ionic species i.

In order to compare the magnitudes of the MHD flow and the jet flow, we estimate the ratio between the Lorentz force and the inertial force, in analogy to the Richardson number discussed in natural convection

[43], which indicates the ratio between the buoyancy and the inertia force:

$$\frac{f_{\mathrm{L}}}{f_{\mathrm{inertia}}} = \frac{jBL}{\rho_0 u^2} \tag{3}$$

Here we take $j = 10000$ A/m^2, $B = 0.4$ T (Fig. 8), $u = u_{\mathrm{inlet}} = 2$ m/s as the characteristic current density, magnetic flux density and velocity, respectively. The characteristic length L is taken to be the length scale of the magnet, $L = 30$ mm. The bulk density ρ_0 is assumed to be 1000 kg/m^3 [44]. The resulting ratio $f_{\mathrm{L}}/f_{\mathrm{inertia}}$ equals 0.03. This indicates that the jet flow is only weakly modified by the Lorentz force. However, it should be noted that the jet flow is directed vertically, while the Lorentz force drives a horizontal MHD flow parallel to the nozzle (in x direction, see Fig. 11b). This additional horizontal flow does not exist in the case without a magnetic field. Therefore, the Lorentz force may exert an influence on the mass transfer at the cathode irrespective of its small magnitude compared to inertia.

As the magnetic field at the machining gap is not uniform, the magnetic gradient force should also be considered. The ratio between the Lorentz force and the magnetic gradient force can be estimated [42]:

$$\frac{f_{\mathrm{L}}}{f_{\nabla \mathrm{B}}} = \frac{\mu_0 j}{\chi_{\mathrm{sol}} \nabla B} \tag{4}$$

The magnetic susceptibility of the solution is calculated to be 5.1×10^{-5} based on the bulk concentration of the paramagnetic metal ions and their molar magnetic susceptibilities, see Eq. 2 [45]. As shown in Fig. 8, a characteristic magnetic field gradient ∇B of 20 T/m is chosen for the main deposition region $(-0.5 \ mm \leq y \leq 0.5 \ mm)$, giving $f_{\mathrm{L}}/f_{\nabla \mathrm{B}} \approx 12$. This indicates that the velocity of the flow caused by the gradient force is less than that of the MHD flow, and both are much weaker than the inlet velocity. According to Eq. 2, the direction of the magnetic gradient force is determined by the direction of the magnetic field gradient. Therefore, the magnetic gradient force may drive a flow towards the edges of the magnets, indicated by the black arrows in the machining gap in Fig. 8. However, this effect is highly localized, only near the edges of the magnets, and appears weak in magnitude compared to the MHD flow caused by the Lorentz force according to the estimation of the force ratio. Therefore, the magnetic gradient force is likely to be only of minor importance and is not considered in the following.

Fig. 9a shows the numerical results of the magnitudes of the Lorentz force and the flow velocity in x, y, z directions averaged in the machining gap. The Lorentz force acts in x direction due to the vertical current density (j_z) and the horizontal magnetic flux density (B_y), see Fig. 11b. Corresponding to the Lorentz force, the MHD flow is directed in x direction and has a magnitude of about 10 mm/s, which is much weaker than the vertical velocity of about 2 m/s. This is in line with the estimated ratio of $f_{\mathrm{L}}/f_{\mathrm{inertia}}$ of about 0.03. Fig. 9b shows U_x along a horizontal line at $y = 0, z = 0.5$ mm (represented by the red line). Without a magnetic field, U_x is zero in the range -5 mm $\leq$ x ≤ 5 mm. This is because when the jet hits the substrate, it splits and leaves the machining gap, mainly in $\pm y$ directions. The flow only has a velocity in x direction near the contact with air $(|x| > 5$ mm$)$, driven by the pressure difference. With the magnetic field, a horizontal MHD flow of $U_x \approx 10$ mm/s is also generated in the middle of the machining gap, which can influence the mass transfer in this region.
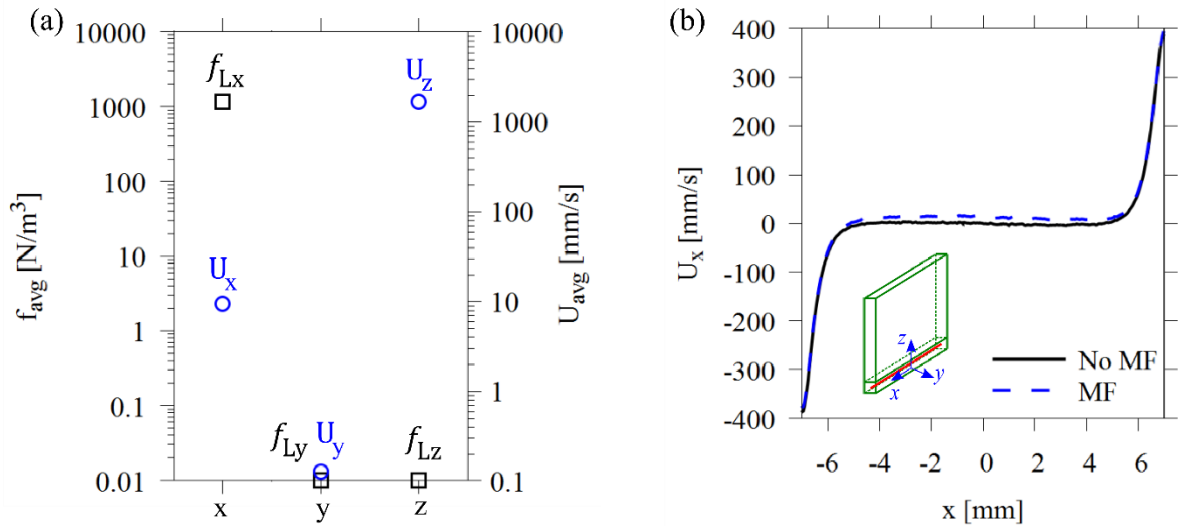
Fig. 9 (a) Magnitudes of the Lorentz force and the flow velocity in x, y, z directions averaged in the machining gap when the magnetic field is applied. The vertical axes are shown on a logarithmic scale. (b) U_x along a horizontal line at $y = 0, z = 0.5$ mm (represented by the red line) with (MF) and without a magnetic field (No MF).

The additional horizontal MHD flow may also affect the flow in y direction. Fig. 10. shows U_y along a horizontal line at $x = 0, z = 0.5$ mm (represented by the red line) with and without a magnetic field. U_y is on the same scale as the inlet jet velocity and is much stronger than the MHD flow. The insets show the velocity of the flow when it leaves the main deposition region ($x \approx \pm 0.5$ mm). It is slightly weaker in the case with the magnetic field on both sides. This mainly appears to be caused by the flow deflection being forced towards the x direction by the Lorentz force, and may result in the ions spending a slightly extended residence time in the main deposition region.
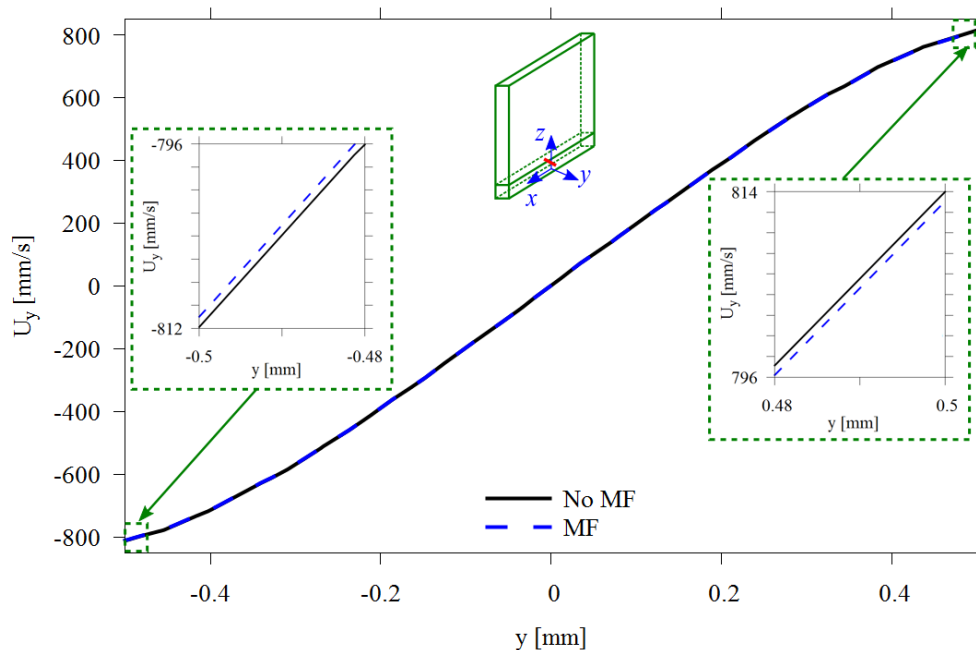

Fig. 10. U_y along a horizontal line at $x = 0, z = 0.5$ mm (represented by the red line) with (MF) and without a magnetic field (No MF).

3.6 Discussion

In the following we discuss in detail how the magnetic field affects the morphology of the deposited layers during jet plating. The two key factors are the magnetic forces, which affect the electrolyte flow and thus the mass transfer, and the crystallization process itself. The main ideas are schematically sketched in Fig. 11.
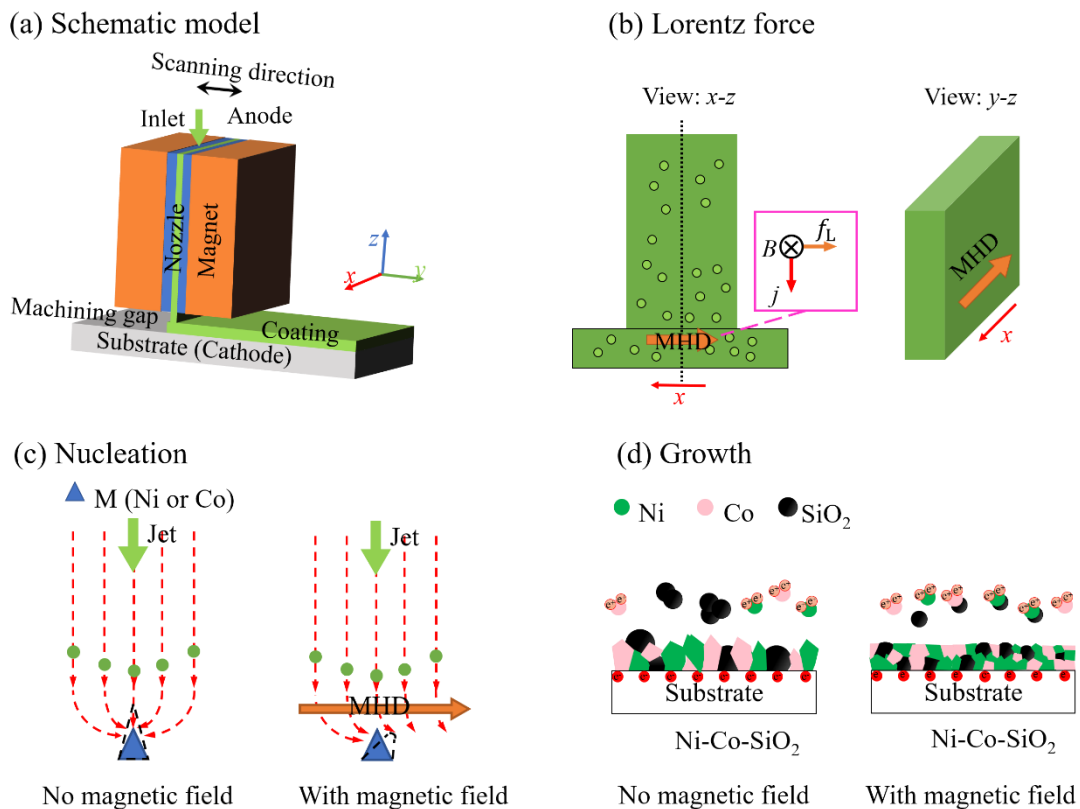

Fig. 11. Schematic views of (a) the magnetic-field-assisted jet plating process, (b) the Lorentz force resulting from the magnetic field, (c) the impact on nucleation and (d) on deposit growth during the deposition.

Electrolyte flow caused by magnetic fields is well known to affect the morphology of the deposited layer [47, 50, 52, 53]. The simulation results of the flow velocities presented above lead us to conclude that below the nozzle, the vertical jet flow (U_z) and the horizontal flow leaving the region (U_y) are superimposed by a horizontal MHD flow with a velocity of $U_x \approx 10$ mm/s, see Fig. 11b. This is unlike the case without a magnetic field. Next, we analyze the possible influence of the MHD flow on the mass transfer [46].

As mentioned above, when the jet flow hits the substrate, it turns horizontally and splits to leave the machining gap. Without magnetic field, for reasons of symmetry, there is no horizontal flow velocity at the stagnation point which is located in the center of the machining gap ($x = 0, y = 0$). However, the magnetic field generates a horizontal MHD flow of $U_x \approx 10$ mm/s which exists also at the stagnation point, see Fig. 9(b). This enhances the convective transport of the Ni²⁺ and Co²⁺ ions, and enriches the concentration boundary layer of the ions, which may lead to the improved uniformity and flatness of the deposit layer

(Fig.11(c-d)) [60]. When moving away from the stagnation point, the horizontal flow velocity U_y rapidly increases and becomes much larger than U_x. There, the magnetic field influences the mass transfer by modifying U_y. As shown in Fig. 10, the flow exits the main deposition region (below the nozzle , $-0.5 \text{ mm} < y < 0.5 \text{ mm}$) with a slightly lower velocity in y direction [48]. This means that the electrolyte with enriched ions is exposed to the main deposition region for a longer time. The extended residence time of the ions near the substrate may also contribute to the refined alloy film. Besides the metal ions, the modified electrolyte flow also enhances the transport of the SiO_2 nanoparticles near the cathode. This may improve the interaction between the nanoparticles and the Ni-Co deposits, which can also contribute to the refinement of the grain growth [23, 25]. Furthermore, the magnetic field can also advance the departure of the hydrogen bubbles from the cathode surface, which enhances the homogeneity of the surface [60].

Besides the electrolyte flow, the magnetic field can also affect the crystallization process. As mentioned earlier, the application of a magnetic field can inhibit the formation of $Co(OH)_2$ and thereby reduce the Co content in the alloy films [32]. This may modify the crystal structure and thus the surface morphology, as can be seen from the XRD results especially for the case with a high Co^{2+} concentration (Fig. 2). It was further found that the magnetic field reduces the crystalline anisotropy, facilitating crystal growth along different directions [49, 54]. Furthermore, during the jet plating, the Ni–Co–SiO$_2$ alloy film became magnetized when exposed to the magnetic field, enabling a dipole-dipole interaction, which inhibited the abnormal aggregation of surface particles during the Ni–Co co-deposition [33]. The reasons mentioned above contributed to the further refinement of the Ni–Co–SiO$_2$ alloy films, obtaining an alloy film with a flatter and a more uniform surface, as shown in Fig. 11d.

The application of a magnetic field is a promising method to enhance the surface morphology of the alloy films especially for the case of large Co^{2+} concentrations. As shown by the SEM photos in Fig. 3, at a high Co^{2+} concentration of 30 g/L, a "smooth" deposit layer can be obtained only if a magnetic field is applied. In future investigations, it would be interesting to study whether the application of magnetic fields enables a route towards smooth and dense alloy layers of higher Co content than possible before.

4 Conclusions

In this article, Ni–Co–SiO$_2$ alloy films were deposited by a new method of jet plating assisted in a magnetic field. For different Co^{2+} concentrations of the electrolyte, the properties of the deposited films were investigated in detail and compared with films obtained without magnetic field. In detail, the texture orientation, the surface morphology, the magnetic properties and the corrosion resistance were investigated. The simulation of the electrolyte flow in the magnetic-field-assisted jet electroplating allowed conclusions to be drawn on how the magnetic field affects the morphology of the deposited alloy film.

It was found that the concentration of Co^{2+} in the electrolyte directly affected the texture orientation of the jet-plated Ni–Co–SiO$_2$ alloy film. At the largest value of 30 g/L investigated here, the Ni–Co–SiO$_2$ alloy film obtained by the conventional method showed a second phase of Co with a hexagonal close-packed structure, whereas film obtained by the assistance of the magnetic field still kept the face-centered cubic structure. This is related to the lower Co content in the films when a magnetic field is applied, which could

be caused by the inhibitated formation of the Co hydroxides due to the electrolyte flow driven by the magnetic forces [32].

In conventional jet plating, in accordance to the texture orientation of the film, the surface morphology changed from a granular structure to a needle-like crystal structure with increasing the Co^{2+} concentration from 10 to 30 g/L. Contrary, in the magnetic-field-assisted jet plating, the films maintained a granular structure for all the concentrations considered in this work, and all films have a smooth, dense surface. This may possibly allow producing smooth and dense layers of higher Co content than obtained so far by the conventional jet-plating method. Furthermore, The magnetic field reduced the crystalline anisotropy and prevented the aggregation of surface particles as the alloy film gets magnetized by the magnetic field . As a result, the growth texture of the alloy film changed, improving the surface morphology of the alloy film.

The change in the composition and the morhpology of the Ni–Co–SiO₂ alloy film influences its magnetic and corrosion properties. The saturation magnetization of the alloy films increased with the increase in the Co^{2+} concentration. A lower coercivity could be obtained in the case of magnetic-field-assisted jet plating. The alloy films obtained by this new method showed the best soft magnetic properties and corrosion resistance at a Co^{2+} concentration of 20 g/L. A coercivity of 7.5 Oe was obtained, which is much lower than the coercivity of ~20 Oe obtained from conventional plating [14, 62]. The corrosion potential was as high as −0.30 V and the corrosion current density was the lowest at 1.12 $\mu A \cdot cm^{-2}$. However, these corrosion properties may depend on the level of dissolved oxygen, which was not explicitly monitored.

Numerical results suggest that the electrolyte flow, being modified by the magnetic forces, influences the mass transfer by locally changing the species and potential distribution, which results in a smoother, denser layer when compared to normal jet plating without applying a magnetic field. The results obtained give support to the experimental results and allow a deeper understanding of the jet plating in a magnetic field. Despite the main effect is based on the Lorentz force, future investigations are intended to consider also the influence of the magnetic gradient force.

It has to be noticed that due to the instabilities caused by the reciprocating scanning movement of the nozzle as well as the high speed of the jet, it is difficult to perform electrochemical measurements of e.g. polarization curves during the deposition, from which information on the mass transfer could be obtained. Therefore, geometric modifications are planned for future work to possibly damp out this instability. Futhermore, limiting current measurements using a well-established redox couple, e.g. $[Fe(CN)_6]^{3-}$ / $[Fe(CN)_6]^{4-}$, would allow to conclude on the mass transfer without substrate motion, from which important insight may be gained.

Acknowledgments

References

[1] N. Zhang, R. Zhao, D. He, Y. Ma, J. Qiu, C. Jin, C. Wang, Lightweight and flexible Ni–Co alloy nanoparticle-coated electrospun polymer nanofiber hybrid membranes for high-performance electromagnetic interference shielding, *J. Alloy. Compd.* 784 (2019) 244–255.

[2] M. M. Balashadehi, P. Nourpour, A. S. R. Aghdam, M. H. Allahyarzadeh, A. Heydarzadeh, M. Hamdi, The formation, microstructure and hot corrosion behaviour of slurry aluminide coating modified by Ni/Ni-Co electrodeposited layer on Ni-base superalloy, *Surf. Coat. Tech.* 402 (2020) 126283.

[3] B. Tóth, L. Péter, Á. Révész, J. Pádár, I. Bakonyi, Temperature dependence of the electrical resistivity and the anisotropic magnetoresistance (AMR) of electrodeposited Ni–Co alloys, *Eur. Phys. J. B* 75 (2010) 167–177.

[4] M. S. Safavi, M. Tanhaei, M. F. Ahmadipour, R. G. Adli, S. Mahdavi, F. C. Walsh, Electrodeposited Ni-Co alloy-particle composite coatings: A comprehensive review, *Surf. Coat. Tech.* 382 (2020) 125-153.

[5] B. Li, W. Zhang, Synthesis of Ni–Co–ZrO_2 nanocomposites doped with ceria particles via electrodeposition as highly protective coating, *J. Alloy. Compd.* 820 (2020) 153158.

[6] A. Karimzadeh, M. Aliofkhazraei, F. C. Walsh, A review of electrodeposited Ni-Co alloy and composite coatings: Microstructure, properties and applications, *Surf. Coat. Tech.* 372 (2019) 463-498.

[7] Anantha R. Sethuraman, A study of preferential sputtering of Ni in Ni-Co alloy films deposited from a single source, *Nucl. Instrum. Meth. B* 54 (1991) 513-517.

[8] P. Scardi, Y. H. Dong, C. Tosi. Co, Ni-base alloy thin films deposited by reactive radio frequency magnetron sputtering. *J. Vac. Sci. Technol. A* 19 (2001) 2394-2399.

[9] D. Kim, K. Aoki, O. Takano, Soft Magnetic Films by Electroless Ni-Co-P Plating, *J. Electrochem. Soc.* 142 (1995) 3763–3767.

[10] J. Pang, Q. Li, W. Wang, X. Xu, J. Zhai, Preparation and characterization of electroless Ni–Co–P ternary alloy on fly ash cenospheres, *Surf. Coat. Tech.* 205 (2011) 4237–4242.

[11] G. M. Chow, J. Ding, J. Zhang, K. Y. Lee, D. Surani, Magnetic and hardness properties of nanostructured Ni–Co films deposited by a nonaqueous electroless method, *Appl. Phys. Lett.* 74 (1999) 1889–1991.

[12] L. Tian, J. Xu, C. Qiang, The electrodeposition behaviors and magnetic properties of Ni–Co films, *Appl. Surf. Sci.* 257 (2011) 4689–4694.

[13] H. Zhou, N. Du, J. Guo, S. Liu, A new insight into promotion action of Co^{2+} in Ni-diamond composite electrodeposition, *J. Mater. Sci. Technol.* 35 (2019) 1797–1802.

[14] A. Karpuz, H. Kockar, M. Alper, O. Karaagac, M. Haciismailoglu, Electrodeposited Ni–Co films from electrolytes with different Co contents, *Appl. Surf. Sci.* 258 (2012) 4005–4010.

[15] B. Li, W. Zhang, D. Li, Synthesis and properties of a novel Ni–Co and Ni–Co/ZrO_2 composite coating by DC electrodeposition, *J. Alloy. Compd.* 821 (2020) 153258.

[16] A. H. El-Sayed, O.M. Hemeda, A. Tawfik, M. A. Hamad, Greatly enhanced magnetic properties of electrodeposited Ni–Co–P–BaFe12O19 composites, *J. Magn. Magn. Mater.* 402 (2016) 105–109.

[17] Z. Chang, J. Gong, C. Sun, Co-based Amorphous/Nanocrystalline Composite Coatings Deposited by

Arc Ion Plating, *J. Mater. Sci. Technol.* 29 (2013) 806–812.

[18] S. Vilain, J. Ebothe, M. Troyon, Surface roughness and composition effects on the magnetic properties of electrodeposited Ni–Co alloys, *J. Magn. Magn. Mater.* 157 (1996) 274–275.

[19] A. Karpuz, H. Kockar, M. Alper, Effect of film thickness on properties of electrodeposited Ni–Co films, *Appl. Surf. Sci.* 258 (2012) 5046–5051.

[20] S. Meena, R. Ashokkumar, E. Ranjith Kumar, Effects of Cr Doping Concentration on Structural, Morphology, Mechanical and Magnetic Properties of Electrodeposited NiCoCr Thin Films, *J. Inorg. Organomet. P.* 29 (2019) 1094–1099.

[21] U. Sarac, M. Baykul, Y. Uguz, The Influence of Applied Current Density on Microstructural, Magnetic, and Morphological Properties of Electrodeposited Nanocrystalline Ni–Co Thin Films, *J. Supercond. Nov. Magn.* 28 (2015) 1041–1045.

[22] G. Qiao, T. Jing, N. Wang, Y. Gao, X. Zhao, J. Zhou, W. Wang, High-speed jet electrodeposition and microstructure of nanocrystalline Ni–Co alloys, *Electrochim. Acta* 51 (2005) 85–92.

[23] W. Jiang, L. Shen, M. Xu, Z. Wang, Z. Tian, Mechanical properties and Corrosion resistance of Ni–Co–SiC composite coatings by Magnetic Field-induced Jet Electrodeposition, *J. Alloy. Compd.* 791 (2019) 847–855.

[24] X. Fu, F. Wang, X. Chen, J. Lin, H. Cao. Corrosion resistance of Ni–P/SiC and Ni–P composite coatings prepared by magnetic field-enhanced jet electrodeposition. *RSC Adv.* 10 (2020) 34167-34176.

[25] B. Li, W. Zhang, Electrochemical Deposition of Ni–Co/SiC Nanocomposite Coatings for Marine Environment, *Int. J. Electrochem. Sci.* 12 (2017) 7017–7030.

[26] Y. Yu, Z. Song, H. Ge, G. Wei, Influence of magnetic fields on cobalt electrodeposition, *Surf. Eng.* 30 (2014) 83–86.

[27] M. Ebadi, W. Basirun, Y. Alias, Influence of magnetic field on the electrodeposition of Ni–Co alloy, *J. Chem. Sci.* 122 (2010) 279–285.

[28] D. Grimmett, M. Schwartz, K. Nobe, Pulsed Electrodeposition of Iron-Nickel Alloys, *J. Electrochem. Soc.* 137 (1990) 3414–3418.

[29] F. J. Fabri Miranda, O. E. Barcia, S. L. Diaz, O. R. Mattos, R. Wiart, Electrodeposition of Zn–Ni alloys in sulfate electrolytes, *Electrochim. Acta*, 41 (1996) 1041–1049.

[30] A. Bai, C.C Hu, T.C. Wen, Composition control of ternary Fe–Co–Ni deposits using cyclic voltammetry, *Electrochim. Acta*, 48 (2003) 2425–2434.

[31] H. Dahms, I. Croll, The Anomalous Codeposition of Iron-Nickel Alloys, *J. Electrochem. Soc.* 112 (1965) 771–775.

[32] J. Koza, M. Uhlemann, A. Gebert, L. Schultz, The effect of a magnetic field on the pH value in front of the electrode surface during the electrodeposition of Co, Fe and CoFe alloys, *J. Electroanal. Chem.* 617 (2008) 194–202.

[33] C. Wu, K. Wang, D. Li, C. Lou, Y. Zhao, Y. Gao, Q. Wang, Tuning microstructure and magnetic properties of electrodeposited CoNiP films by high magnetic field annealing, *J. Magn. Magn. Mater.* 416 (2016) 61–65.

[34] G. Herzer, Grain size dependence of coercivity and permeability in nanocrystalline ferromagnets, *IEEE*

Trans. Magn. 26 (1990) 1397–1402.

[35] P. Hu, Z. Chen, T. Chang, J. Deng, F. Yang, K. Wang, Q. Li, B. Hu, H. Yu, W. Wang, Magnetic properties of the nanoscale coral-shaped Ni–Co alloy powder with different Co contents, *J. Alloy. Compd.* 727 (2017) 332–337.

[36] S. Mehrizi, M. Sohi, S. Ebrahimi, Study of microstructure and magnetic properties of electrodeposited nanocrystalline CoFeNiCu thin films, *Surf. Coat. Tech.* 205 (2011) 4757–4763.

[37] G. Meng, Y. Li, Y. Shao, T. Zhang, Y. Wang, F. Wang, X. Cheng, C. Dong, X. Li, Effect of Microstructures on Corrosion Behavior of Nickel Coatings: (I) Abnormal Grain Size Effect on Corrosion Behavior, *J. Mater. Sci. Technol.* 31 (2015) 1186–1192.

[38] C.U. Atuanya, D. I. Ekweghiariri, C.M. Obele, Experimental study on the microstructural and anti-corrosion behaviour of Co-deposition Ni–Co–SiO$_2$ composite coating on mild steel, *Def. Technol.* 14 (2018) 64–69.

[39] Y. Wang, S. Tay, S. Wei, C. Xiong, W. Gao, R. Shakoor, R. Kahraman, Microstructure and properties of sol-enhanced Ni–Co–TiO$_2$ nano-composite coatings on mild steel, *J. Alloy. Compd.* 649 (2015) 222–228.

[40] COMSOL Multiphysics Documentation Suite V 5.5, *Burlington*, MA 01803, USA (2019).

[41] M. Huang, G. Marinaro, X. Yang, B. Fritzsche, Z. Lei, M. Uhlemann, K. Eckert, G. Mutschke, Mass transfer and electrolyte flow during electrodeposition on a conically shaped electrode under the influence of a magnetic field, *J. Electroanal. Chem.* 842 (2019) 203–213.

[42] G. Mutschke, K. Tschulik, T. Weier, M. Uhlemann, A. Bund, J. Fröhlich, On the action of magnetic gradient forces in micro-structured copper deposition, *Electrochim. Acta* 55 (2010) 9060–9066.

[43] A. A. Grachev, C. W. Fairall, Dependence of the Monin–Obukhov Stability Parameter on the Bulk Richardson Number over the Ocean, *J. Appl. Meteorol. Climatol.* 36 (1997) 406–414.

[44] D. R. Lide, *CRC handbook of chemistry and physics*, Vol. 85, CRC press (2004).

[45] J. Coey, F. Rhen, P. Dunne, S. McMurry, The magnetic concentration gradient force – is it real, *J. Solid State Electr.* 6 (2007) 711–717.

[46] B. J. Kirby, Micro- and Nanoscale Fluid Mechanics: Transport in Microfluidic Devices. *Cambridge university press* (2010).

[47] R. Morimoto, A. Sugiyama, R. Aogaki, Nano-scale Crystal Formation in Copper Magneto-electrodeposition under Parallel Magnetic Fields, *Electrochemistry* 72 (2004) 421–423.

[48] R. Aogaki, R. Morimoto, M. Asanuma, Nonequilibrium fluctuations in micro-MHD effects on electrodeposition, *J. Magn. Magn. Mater.* 322 (2010) 1664–1668.

[49] X. Li, Y. Fautrelle, Z. Ren, Influence of a high magnetic field on columnar dendrite growth during directional solidification, *Acta Mater.* 55 (2007) 5333–5347.

[50] A. Bund, A. Ispas, G. Mutschke, Magnetic field effects on electrochemical metal depositions, *Sci. Technol. Adv. Mater.* 9 (2008) 024208.

[51] M. Huang, K. Eckert, G. Mutschke, Magnetic-field-assisted electrodeposition of metal to obtain conically structured ferromagnetic layers, *Electrochim. Acta* 365 (2020) 137374.

[52] K. Tschulik, R. Sueptitz, J. Kozq, M. Uhlemann, G. Mutschke, T. Weier, A. Gebert, L. Schultz, Studies on the patterning effect of copper deposits in magnetic gradient fields, *Electrochim. Acta* 56 (2010) 297–304.

[53] V. Ganesh, D. Vijayaraghavan, V. Lakshminarayanan, Fine grain growth of nickel electrodeposit: effect of applied magnetic field during deposition, *Appl. Surf. Sci.* 240 (2005) 286–295.

[54] S. V. Kovalyov, O. B. Girin, C. Debiemme-Chouvy, V. I. Mishchenko, Copper electrodeposition under a weak magnetic field: effect on the texturing and properties of the deposits, *J. Appl. Electrochem.* 51 (2021) 235-243.

[55] K. Abe, T. Kondoh, Y. Nagano, A new turbulence model for predicting fluid flow and heat transfer in separating and reattaching flows – I. Flow field calculations, *Int. J. Heat Mass Transfer* 37 (1994) 139–151.

[56] K. C. Das, D. Panda, S. K. Singh, Densities and Viscosities of $NiSO_4$–H_2SO_4–H_2O system, *Phy. Chem. Liq.* 32 (1996) 123–126.

[57] L. F. Moody, Friction Factors for Pipe Flow. *Transactions of the A. S. M. E.* (1944) 671–684.

[58] A. J. Bard and L. R. Faulkner, Electrochemical Methods, 2nd ed., *John Wiley & Sons*, 2001.

[59] M. S. Moats, J. B. Hiskey, D. W. Collins, The effect of copper, acid, and temperature on the diffusion coefficient of cupric ions in simulated electrorefining electrolytes, *Hydrometallurgy* 56 (2000) 255–268.

[60] M. Uhlemann, K. Tschulik, A. Gebert, G. Mutschke, J. Fröhlich, A. Bund, X. Yang, K. Eckert, Structured electrodeposition in magnetic gradient fields, *the European Physical Journal Special Topics* 220 (2013) 287–302.

[61] W. Jiang, M. Qiu, L. Shen, G. Lou, X. Yang, K. Eckert, Z. Tian, Effect of deposition current density on the Co–Ni/SiO2 alloy composite coatings Using Scanning Jet Electrodeposition, *Surf. Topogr.: Metrol. Prop.* 9 (2021) 015027.

[62] D. Kim, D. Y. Park, B. Y. Yoo, P. T. A. Sumodjo, N. V. Myung, Magnetic properties of nanocrystalline iron group thin film alloys electrodeposited from sulfate and chloride baths, *Electrochim. Acta* 48 (2003) 819–830.